A spectral model of the FeO orange bands with a comparison between a laboratory spectrum and a night airglow spectrum observed by OSIRIS on Odin

R.L. Gattinger, W.F.J. Evans, D.A. Degenstein, and E.J. Llewellyn

Abstract: Emissions from the FeO orange bands have been observed in the laboratory for many decades. The transition has been identified as $D(^5\Delta_i)$–$X(^5\Delta_i)$ where the subscript identifies the five Ω spin components. While the ground-state molecular constants are well-known, information on the upper state is less precise, and this is primarily due to significant energy level perturbations. Using the available constants, a preliminary spectral simulation model of the orange bands has been developed with a wavelength accuracy of approximately 1/3 nm. Using data from the OSIRIS spectrograph on board the Odin spacecraft, these FeO orange bands have been identified as a component of the night airglow spectrum emanating from the upper mesosphere. The spectral simulation model is combined with the OSIRIS observations to determine the vibrational development of the FeO emissions in the airglow. The model is also applied to published laboratory observations of the orange bands, conducted at much higher pressure than for the airglow, to test for different vibrational development.

PACS Nos: 33.20.Kf, 34.50.Ez, 92.60.H-, 92.60.hb, 92.60.hc, 92.60.hw, 95.30.Ft, 95.30.Fg, 95.30.Kr

Résumé : Pendant des décennies, nous avons observé en laboratoire les bandes dans l'orange du FeO. La transition a été identifiée comme étant $D(^5\Delta_i)$–$X(^5\Delta_i)$, où l'indice inférieur identifie la composante Ω du spin. Alors que les constantes moléculaires du fondamental sont bien connues, celles de l'état supérieur le sont moins, largement à cause des perturbations entre les niveaux. Utilisant les constantes disponibles, nous avons développé un modèle préliminaire simulant ces bandes avec une précision sur la longueur d'onde de 1/3 nm. À l'aide des données du spectrographe OSIRIS à bord du satellite Odin, nous avons identifié ces bandes dans l'orange comme une composante de la lueur atmosphérique nocturne émanant de la mésosphère supérieure. Le modèle de simulation spectrale est combiné avec les observations d'OSIRIS pour obtenir le développement vibrationnel des émissions de FeO dans la lueur. Nous utilisons aussi le modèle en conjonction avec des mesures publiées, obtenues en laboratoire à une pression beaucoup plus élevée que dans la mésosphère, afin de vérifier différents développements vibrationnels.

[Traduit par la Rédaction]

1. Introduction

The study of the terrestrial night airglow dates back more than a century to the first measurement of the wavelength of the mysterious "green line" by Ångström [1], reported as 556.7 nm. The source of the green emission was identified by McLennan and Shrum [2] as a transition from the OI metastable $^1S_0$ state to the $^1D_2$ state. Barbier et al. [3] established the presence of an underlying terrestrial based continuum in the airglow, which is in addition to the star background and zodiacal light inherent in ground-based observations. Sternberg and Ingham [4] evaluated the contin-

uum differential brightness at a series of wavelengths in the visible and near infrared from their spectrometric observations. They found the continuum peaks at around 600 nm and noted the similarity to the $NO + O \rightarrow NO_2^*$ chemiluminescent air afterglow spectrum. A number of rocket-borne observations of this NO_2^* air afterglow emission have been made at high latitudes [5–8]. Gattinger et al. [9] found that the NO_2^* night airglow emission is much brighter at polar latitudes than at low latitudes. Cosby and Slanger [10] presented a night sky spectrum obtained from the echelle spectrograph and imager (ESI) on the Keck II telescope on Mauna Kea, $20°$ north latitude, which shows a structured continuum in the 550 to 650 nm region that does not match the spectral shape of the chemiluminescent $NO + O \rightarrow NO_2^*$ emission [11].

Evans et al. [12] observed this unidentified spectral feature in the night airglow using a space-borne spectrograph in limb tangent viewing mode. By subtracting spectra obtained above the main airglow layer, they removed the stellar and zodiacal light background and so isolated the airglow component. After removal of known airglow emission features, particularly the OH Meinel vibration–rotation bands, the spectral shape in the 600 nm region was observed

R.L. Gattinger,[1] D.A. Degenstein, and E.J. Llewellyn. ISAS, Department of Physics and Engineering Physics, University of Saskatchewan, Saskatoon, SK S7N 5E2, Canada.
W.F.J. Evans. NorthWest Research Associates, Inc, 4118 148 Ave. NE, Redmond, WA, 98052, USA; Centre for Research in Earth and Space Science, York University, 4700 Keele Street, Toronto, ON M3J 1P3, Canada.

[1]Corresponding author (e-mail: gattinger@rogers.com).

to be very similar to the structured pseudo-continuum observed in both a Leonid meteor persistent train and in a laboratory spectrum of the FeO orange bands [13]. Further, by positive correlation with the Na airglow emission in both intensity and altitude distribution, they identified the 600 nm feature as arising from the FeO orange bands.

As is the case with atomic hydrogen, both Fe and Na form catalytic cycles with O and O_3, thereby destroying the odd O as well as playing significant roles in ion chemistry in the mesopause region [14, 15]. In addition, the temporal and spatial distributions of Fe and Na can be used as tracers of atmospheric dynamics [16].

To extend the analysis of the FeO orange bands, a spectral simulation model has been developed using laboratory determinations of the molecular constants of the upper and lower states. The model is also used to investigate the vibrational development of both the observed FeO airglow and the laboratory spectra. Finally, a tabulated model spectrum with 1/10 nm bins is presented as an appendix.

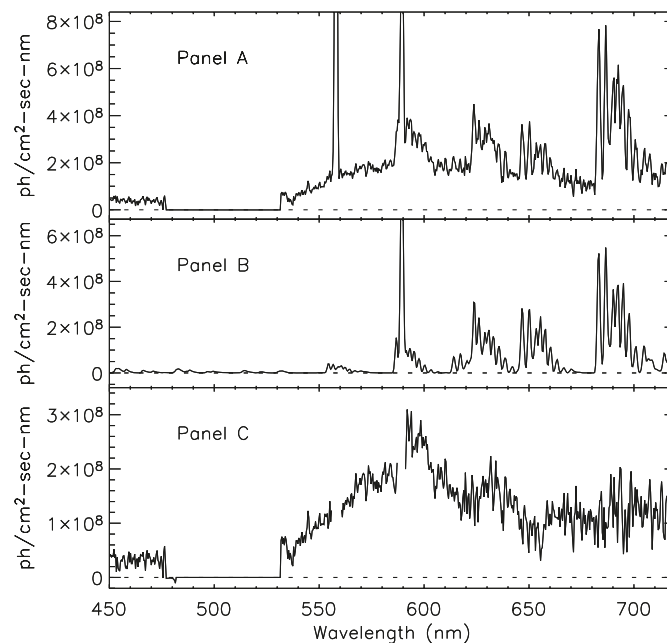## 2. FeO orange bands observed in the night airglow

The airglow observations presented here were made with the optical spectrograph and infrared imager system (OSIRIS) [17] on the Odin spacecraft [18] that was launched on 20 February 2001. The ascending node is nominally at 1800 Local Time, and the orbit inclination 97.8°. The tangent limb is scanned vertically at approximately 0.75 km s^{-1} with a field of view of 1 km and exposure times typically 2 s. The limb tangent point absolute pointing knowledge is known to better than one-half kilometre.

The full 275 to 815 nm wavelength range is exposed simultaneously with a spectral resolution of approximately 0.90 nm. Accurate relative spectral calibration of the OSIRIS instrument is essential to obtain reliable emission ratios. Prelaunch calibrations with standard lamps are the basis of the calibration, supplemented on-orbit with astronomical observations. The absolute calibration error is ±10% and the precision approximatley 5%. On-orbit daytime limb scatter spectra are combined with simulations using the SASKTRAN three-dimensional radiative transfer model described by Bourassa et al. [19] to refine the calibrations during the mission.

Spectra from individual limb scans are analyzed over the 75 to 105 km limb tangent altitude range. For each limb scan, a slowly changing CCD dark pattern is determined from the exposures in the 105 to 110 km tangent altitude range and subtracted from the observed tangent limb spectra. This background subtraction procedure automatically removes any non-terrestrial emission sources, including zodiacal light and integrated light from stars [4]. The effects of scattered solar radiation were excluded by using only those spectra for which the solar zenith angle was greater than 101°.

An averaged airglow spectrum from 450 to 720 nm, limb altitude range from 80 to 92 km, is shown in Panel A of Fig. 1. This averaged spectrum is from latitudes between the Equator and 40° South over five 24 h observing periods between 20 April 2003 and 27 May 2003. Latitudes poleward of 40° have been excluded to minimize the contribution of the chemiluminescent $NO + O \rightarrow NO_2^*$ reaction [20] that arises from enhanced NO in the dark polar regions [9]. Fol-

Fig. 1. Panel A is an averaged night airglow spectrum observed by OSIRIS. Panel B is the fitted model spectrum that includes two O_2 atmospheric bands between 700 and 720 nm, the obvious OH Meinel bands and weak Herzberg bands. The oxygen green line at 557.7 nm is omitted in Panel B. Panel C is Panel A minus Panel B and clearly reveals the very weak FeO range band airglow emission. The data are from April and May of 2003, averaged from 80 to 92 km. Data within the range of the OSIRIS order sorter from 480 to 530 nm are absent.

lowing the procedures described by Evans et al. [12], the modeled night airglow spectrum is show in Panel B (Fig. 1). The Meinel OH bands have been modeled using the relative band intensities determined by Cosby and Slanger [10] and the line strengths of Langhoff et al. [21]. Similarly, emissions from the O_2 ($b^1\Sigma_g^+ - X^3\Sigma_g^-$) system have been modeled using the relative band intensities determined by Slanger et al. [22]. Also, in the blue spectral region, the O_2 Herzberg and Chamberlain emissions have been estimated using the tabulations of Cosby et al. [23]. The residual spectrum determined by subtracting the modeled spectrum (Fig. 1, Panel B) from the observed spectrum (Fig. 1, Panel A) is shown in Panel C of Fig. 1. It should be noted that the spectral regions containing the bright atomic emissions in the upper curve, OI ($^1S-^1D$) at 557.7 nm and the Na doublet centred on 589.3 nm, have been omitted in the lowest spectrum. Evans et al. [12] identified the main features in the residual spectrum as arising from the FeO orange bands. The spectral nature of these bands is investigated in more detail in the following sections.

3. Spectral simulation of the FeO orange bands

The FeO orange bands arise from a $^5\Delta_i - ^5\Delta_i$ electronic transition [24]. The molecular constants for the $X(^5\Delta_i)$ ground state and the formulae for calculating the energy levels of the five Ω spin components have been tabulated by Cheung et al. [25] and Taylor et al. [26]. For the upper state of the orange bands, Barnes et al. [27] determined that there

are two electronic systems involved, which they called $D(^5\Delta_i)$–$X(^5\Delta_i)$ and $D'(^5\Delta_i)$–$X(^5\Delta_i)$. They placed the origin of the $\Omega = 4$ spin component for the newly identified D'–X system at 611 nm and they provided approximate molecular constants. For the D–X system, the experimental results of Son et al. [28] suggest the origin is at the 591.1 nm band, an assignment that yields qualitative agreement with the published locations of band heads. However, the actual band assignments remain uncertain [29].

In the present work, band origins for the five Ω spin components have been calculated for transitions from a range of upper vibrational levels to a range of ground-state vibrational levels. Only $\Delta\Omega = 0$ transitions are included in this initial analysis. Rotational energy level differences from the upper state to the lower state have been calculated for each of the vibrational bands for the R, Q, and P branches. Approximate values of the line strengths, S_J, for the R, Q, and P branches of the FeO orange bands have been inferred from the rotationally resolved spectra obtained by Barnes et al. [27] at a known emitting temperature. These provisional experimental line strengths are similar to the classical Hönl–London values [30].

A model spectrum of the D–X 0–0 band in the 592 nm region is shown in Fig. 2 for an assumed temperature of 200 K. The five Ω spin components are apparent, each is assumed to be of equal brightness for this initial simulation (see below). For each Ω component, the R and Q branches are concentrated within a span of approximately 1 nm, while the P branch extends over approximately 4 nm. The full width of each band, over the five Ω components, is about 10 nm. The calculated band positions for the brighter bands of the D–X system, from approximately 500 to 750 nm, are listed in Table 1. The reference wavelengths for each band is the $\Omega = 4$ spin component and the $R_4(10)$ rotational line position, which is typically near the R branch head. For example, from Table 1 the 0–0 band is located at 591.3 nm, in agreement with the location of the $\Omega = 4$ R branch head in Fig. 2. Wavelengths for bands with v' and v'' less than approximately three are expected to be accurate to ~ 0.1 nm, but are more uncertain for higher values because of decreased accuracy of the molecular constants. Perturbations of the upper energy levels are not included in the model, since, considering the OSIRIS measurement accuracy, they are not expected to affect the analysis presented in the following sections.

A model spectrum for the D′–X 0–0 band is shown in Fig. 3. Again, the R, Q, and P branches are apparent, but for each band there is a marked difference in the wavelength distribution of the five Ω components compared with the D–X system shown in Fig. 2. The $\Omega = 4$ R(10) wavelengths for the D′–X bands are also listed in Table 1.

The next step in the model simulation of the FeO orange bands is to determine the relative intensities for each of the bands by comparing with the observed spectra. For the orange bands, in emission the relative intensities of the five Ω components in a given band are essentially equal [24]. Similarly, from the Cheung et al. measurements [25] it appears that bands in the D′–X system have approximately the same intensity as those in the D–X system, a simplification that is assumed in the present simulation. As a result, the band intensities derived in the next section are an average of the two systems.

Fig. 2. Simulated spectrum of the FeO D–X band at 5920 Å. The individual rotational lines in the R ($\diamond$), Q (*), and P ($\square$) branches are indicated.
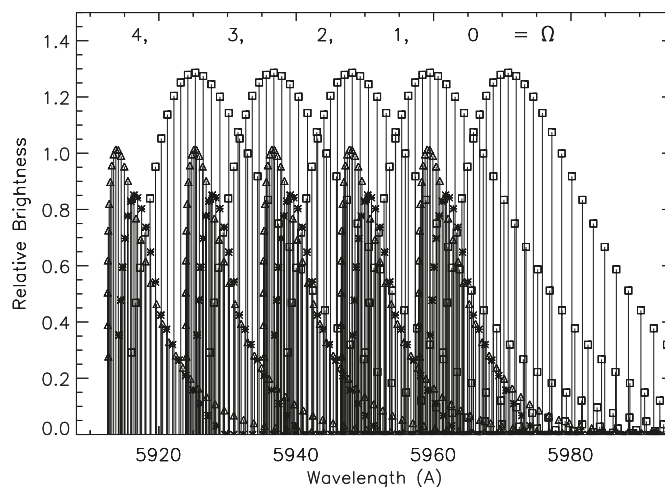
Franck–Condon factors, which specify the relative band intensities within a given v' progression, do not appear to be available for the internuclear distances of the D and D′ upper states determined by Barnes et al. [27]. If Franck–Condon factors were available, the precision of the present spectral simulation could be improved. As a tentative solution since the internuclear distances are similar, it is assumed that the relative band intensities within a given v' progression are the same for both D–X and the D′–X systems. The final band intensities are then determined iteratively by matching the model spectrum against the available experimental spectra.

The maximum attainable energy levels in the excited FeO molecules arising from the $Fe + O_3 \rightarrow FeO + O_2$ reaction are limited by energy balance considerations. Helmer and Plane [31] have indicated that the reaction is exothermic by 307 ± 8 kJ mol^{-1}. From electronic and vibrational term value sums calculated using constants derived by Barnes et al. [27], the maximum upper state vibrational levels for the D′ and D systems are $v' = 10$ and $v' = 12$, respectively. These limits have been assumed for the band simulations described below.

The contribution from FeO isotopologues, other than ^{56}FeO, to the total emission is expected to be approximately 8% [24]. The measured isotopic shifts in band locations are less than approximately 0.1 nm, significantly smaller than the 0.9 nm resolution of the OSIRIS spectra. Thus, the effects of isotopic shifts are not included in the present model.

In summary, the objective here is to derive the relative band intensities within the observed spectra of the FeO orange bands using the model and so identify the spectral components that contribute to the observed total emission at each wavelength. The application of the spectral model to the observed FeO orange bands is discussed in the next section.

4. Comparison between model and observed FeO orange bands

The observational data for comparison with the model discussed in the previous section include the OSIRIS FeO night airglow spectrum shown in Fig. 1, Panel C (repeated

Table 1. Deslandres table for FeO orange bands with wavelengths (nm) of the $\Omega = 4$ R(10) rotational lines and relative band intensities.

v''/v'	0	1	2	3	4	5	6	7	8	9	10	11	12
0	591.3 611.1 0.80	623.4 645.5 0.30	658.7 683.5 0.07	697.9 725.7 0.04	741.5. 773.0 (0.02)								
1	568.9 582.2 0.09	598.5 613.3 0.34	631.0 647.5 0.26	666.9 685.3 0.17	706.6 727.3 0.12	750.8 727.3 (0.09)							
2	548.2 556.2 0.18	548.2 584.5 0.36	605.7 615.5 0.45	638.6 649.6 0.27	674.9 687.2 0.18	715.2 728.9 0.09	760.0 775.5 (0.05)						
3	529.1 532.8 0.16	554.6 558.7 0.38	582.4 586.9 0.88	612.8 617.8 0.38	646.2 651.7 0.30	683.0 689.1 0.25	723.7 730.6 0.15	769.0 776.8 (0.06)					
4	511.4 511.4 0.03	535.2 535.3 0.26	561.0 561.1 0.85	589.2 589.3 0.68	619.9 620.1 0.51	653.7 653.9 0.31	690.9 691.1 0.26	732.1 732.3 0.17	778.0 778.2 (0.09)				
5		517.1 514.0 0.01	541.2 537.8 0.02	567.4 563.6 0.33	595.9 591.7 1.10	627.0 622.4 0.66	661.2 656.1 0.38	698.8 693.1 0.33	740.5 734.1 (0.17)				
6		500.4 494.6 0.01	522.9 516.6 0.04	547.3 540.4 0.07	573.7 566.2 0.36	602.5 594.2 0.54	634.0 624.8 0.45	668.6 658.3 0.27	706.6 695.2 0.23	748.7 735.9 (0.18)			
7			505.9 497.3 0.01	528.7 519.3 0.03	5533 543.0 0.06	580.0 568.8 0.40	609.2 596.8 0.48	641.0 627.2 0.40	675.9 660.6 0.32	714.3 697.3 0.24	756.8 737.8 (0.16)		
8					534.4 522.0 0.01	559.3 545.7 0.02	586.3 571.4 0.12	615.7 599.3 0.42	647.8 629.7 0.36	683.1 663.0 0.30	721.8 699.5 0.24	764.8 739.7 (0.18)	
9					516.8 502.8 0.01	540.1 524.8 0.02	565.2 548.5 0.06	592.5 574.1 0.11	622.2 602.0 0.17	654.6 632.3 0.28	690.1 665.4 0.55	729.3 701.7 0.28	772.6 741.6 (0.17)
10						522.2 505.6 0.01	545.7 527.6 0.02	571.1 551.3 0.05	598.6 576.9 0.10	628.6 604.6 0.15	661.3 634.8 0.25	697.1 667.8 0.50	736.6 703.9 0.25
11							527.6 — 0.01	551.3 — 0.02	576.9 — 0.05	604.7 — 0.10	634.9 — 0.15	667.9 — 0.25	704.0 — 0.50
12								532.9 — 0.01	556.8 — 0.02	582.7 — 0.05	610.7 — 0.10	641.1 — 0.15	674.0 — 0.25

Note: In each cell: (top row) D–X wavelengths, (middle row) D′–X wavelengths, (bottom row) relative band intensities observed in the night airglow; intensities in brackets indicate extrapolated values.

in Fig. 4) and the laboratory fast flow tube spectrum of Jenniskens et al. [13], shown in Fig. 5. The spectral peaks in the laboratory spectrum are located slightly shortwave relative to the peaks observed in the airglow spectrum. Jenniskens et al. [13] have noted that "the relative heights and shapes of the three dominant FeO peaks may be somewhat different at low pressure when quenching is absent". This difference between the two observed spectra is investigated here.

Simulations are performed simultaneously on the airglow and laboratory spectra to determine mutually satisfactory relative band intensities within each v' progression for both observed spectra (see discussion of Franck–Condon factors above). This iteration is interleaved with an uncoupled determination of the relative populations in each upper vibrational level for the two observed spectra. As noted previously, the band intensities for the D–X and the D'–X systems are assumed to be equal.

The comparison between the model spectrum and the observed airglow spectrum is shown in Fig. 4. The corresponding relative band intensities are included in Table 1. The model spectrum has been summed into 0.1–nm bins and then convolved with the 0.9 nm spectral resolution of the OSIRIS observations for the comparison. The brightest bands tend to fall near the $\Delta v = 0$ locus (Table 1); this is to be expected, since the internuclear distances for the D, D', and X states are all very similar [27]. Despite the many degrees of freedom available in the fitting procedure, changes of approximately 20% in the brighter bands result in a much degraded spectral match between the model and the observed spectra. In addition, the pronounced decrease in observed intensity with decreasing wavelength places clear upper limits on even the weaker bands to the left of the $\Delta v = 0$ diagonal, which corresponds to the shorter wavelengths. The correlation coefficient between the model and observed spectra shown in Fig. 4 is 0.83, indicates a 69% coefficient of determination. The measurment noise that is apparent in the OSIRIS spectrum shown in Fig. 4 has the effect of reducing the correlation coefficient. By smearing the OSIRIS spectrum over 2 nm to reduce the noise, the correlation coefficient with the model spectrum increases to 0.89, indicating an 80% coefficient of determination.

The comparison between the model and the experimental results of Jenniskens et al. [13] is shown in Fig. 5. In this case the binned 0.1 nm model spectrum is convolved with the approximately 2.2 nm spectral resolution of the laboratory spectrum [13]. As described above, the relative intensities of bands within individual v' progressions are as given in Table 1, but the relative vibrational populations are determined iteratively in the spectral fitting procedure. The correlation coefficient between the modeled and observed spectra shown in Fig. 5 is 0.86, this indicates a 74% coefficient of determination.

A more detailed example of how the FeO vibrational development in the D' and D states leads to the model spectrum is shown in Fig. 6. The spectral region from 615 to 658 nm that has been chosen as the airglow spectrum differs considerably from the laboratory spectrum in this region. For the simulated laboratory spectrum, the band intensities, represented by the sizes of the square symbols, decrease rapidly from $v' = 0$ to $v' = 5$. For the simulated airglow spectrum,

Fig. 3. Simulated spectrum of the FeO D'–X band at 6110 Å. The individual R, Q, and P rotational lines are plotted as in Fig. 2.
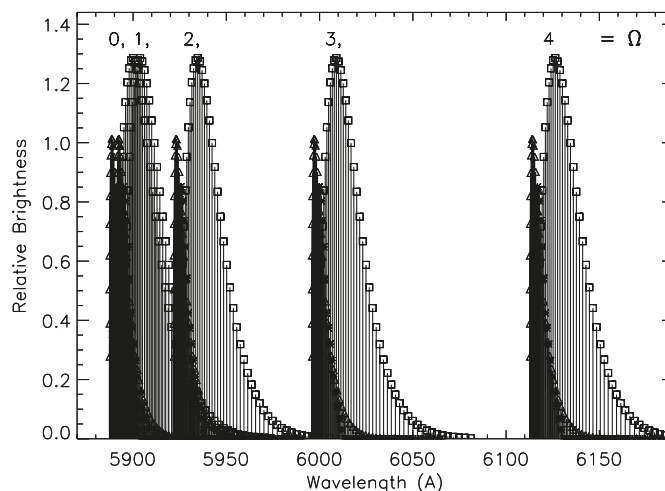
Fig. 4. Simulated spectrum of the FeO orange bands compared with the observed night airglow spectrum (Fig. 1 Panel C). The observed spectrum contains an obvious noise component.
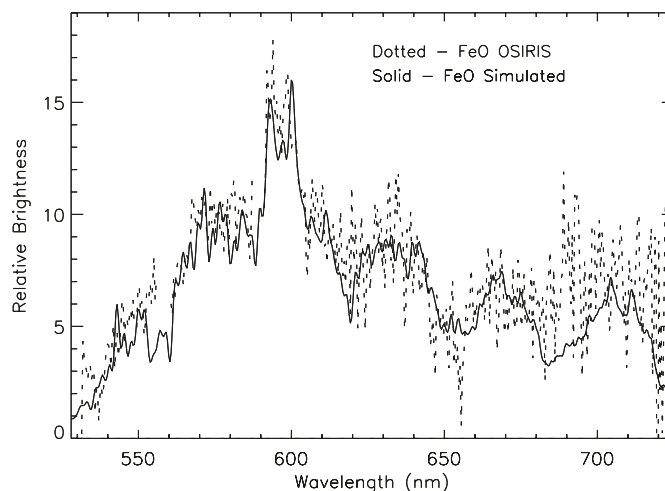
Fig. 5. Simulated spectrum of the FeO orange bands compared with the spectrum observed in laboratory (shifted to the red by 1 nm).
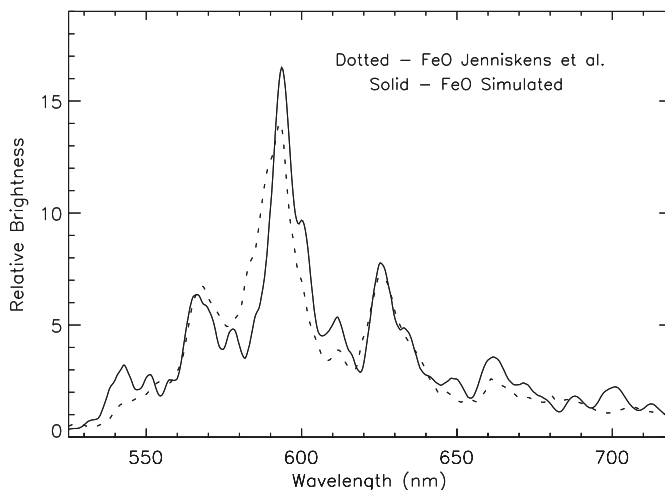
the band intensities, represented by the sizes of the plus signs, extend to much higher v' levels. This difference arises as the observed features extend to longer wavelengths in the airglow spectrum. For example, in the 640 nm region the higher v' levels contribute most of the emission. Because of the closely spaced nature of the spin components and the presence of many bands, the FeO orange spectrum appears to be a pseudo-continuum at typical airglow observing spectral resolution.

The vibrational term values for the D′ and the X states are very similar and so result in closely spaced bands in each sequence; this is apparent in Fig. 6. Conversely, the D state vibrational term increments are significantly different and so result in more widely spaced bands within each sequence.

A comparison between the vibrational development of the two experimental spectra, as determined from the spectral matching results shown in Figs. 4 and 5, is shown in Fig. 7. The band intensity sums in each upper level for the airglow simulation (from Table 1) are compared with those derived for the laboratory spectrum. The error bars are based on the estimated precision of the match between the observed and modeled spectra. It is apparent that the airglow spectrum is populated to significantly higher v' levels than is the laboratory spectrum. This difference in vibrational development between the two FeO spectra is discussed in the next section.

6. Discussion and conclusions

As demonstrated in the previous section, the vibrational development of the FeO orange bands observed in the airglow is considerably enhanced relative to that observed in the laboratory spectrum. One of the major differences between the two observations is the ambient pressure. For the laboratory observations, the pressure in the reaction vessel was approximately 1 mb [13] or 100 Pa. For the airglow spectrum, the pressure in the mesopause region is approximately 0.2 Pa. The corresponding inter-collision times between ambient molecules are approximately 100 ns and 200 μs, respectively. The measured natural lifetime of the FeO ($^5\Delta_i$) upper state is approximately 400 ns, this value is averaged over a number of bands [28]. Accordingly, because in the mesopause region the radiative lifetime is considerably shorter than the inter-collision interval, the impact of collisional redistribution is expected to be minor. However, under laboratory conditions the collision rate exceeds the rate of radiation by factor of four and thus opens the possibility of collisional redistribution.

By analogy, collision-induced vibrational redistribution has been investigated extensively for the airglow OH ($^2\Pi$–$^2\Pi$) vibration–rotation band system [32, 33]. From these analyses, collisional redistribution accounts for approximately one-half of the total loss from the higher v' states at an altitude of 90 km, the other half occurs via radiation. The rate of vibrational relaxation is highly dependent on vibrational level, increasing by more than two orders of magnitude from $v'=1$ to $v'=9$ [34]. For $v'=9$, the vibrational redistribution efficiency, predominantly driven by O_2, is approximately one-tenth of gas kinetic. Xue et al. [35] observed a similar strong dependence of the relaxation rate with vibrational excitation using SO_2 and collision partners. Following the above discussion, for FeO excited under the laboratory conditions the radiative lifetime is approximately

Fig. 6. Simulated night airglow spectrum (solid) compared with simulated laboratory spectrum (dots), including both the D–X and the D′–X systems. The locations of the R branch heads for the five spin components in each band are shown. The symbol size is proportional to the simulated band intensity (+ for airglow, □ for laboratory). Each group of five symbols in a band represents the complete rotational line stucture similar to that shown in Figs. 2 and 3. The lower group of vibrational transition designations is for the D–X (v', v'') bands, with labels to the right of the $\Omega = 0$ subset (see Fig. 2). The upper group is for the D′–X (v', v'') bands with labels to the left of the $\Omega = 4$ subset (see Fig. 3).
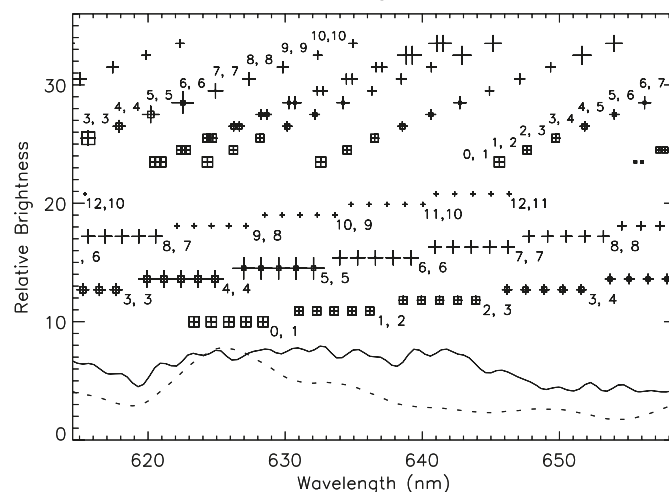
Fig. 7. Comparison of the FeO orange bands upper state vibration relative intensities between night airglow and laboratory observations.
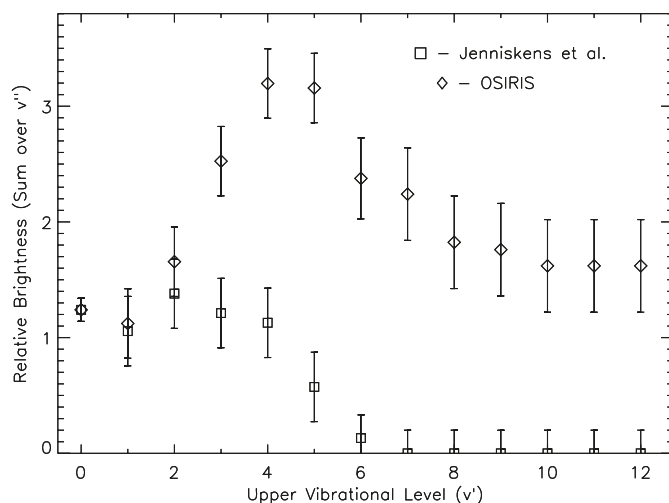
four times the inter-collision interval, while in the mesopause region it is much less. This suggests that the collisional relaxation efficiency for FeO is probably near gas kinetic if it is to have the major effect shown in Fig. 7.

References

1. A.J. Ångström. Pogg. Ann. **213**, 161 (1869). doi:10.1002/andp.18692130510.
2. J.C. McLennan and G.M. Shrum. Proc. R. Soc. Lond. A, **108**, 501 (1925). doi:10.1098/rspa.1925.0088.
3. D. Barbier, J. Dufay, and D. Williams. Ann. Astrophys. (Paris), **14**, 399 (1951).
4. J.R. Sternberg and M.F. Ingham. Mon. Not. R. Astron. Soc. **159**, 1 (1972).
5. W.E. Sharp. J. Geophys. Res. **83**, A9, 4373 (1978). doi:10.1029/JA083iA09p04373.
6. G. Witt, J. Stegman, B.H. Solheim, and E.J. Llewellyn. Planet. Space Sci. **27**, 341 (1979). doi:10.1016/0032-0633(79)90111-9.
7. G. Witt, J. Rose, and E.J. Llewellyn. J. Geophys. Res. **86**, A2, 623 (1981). doi:10.1029/JA086iA02p00623.
8. I.C. McDade, E.J. Llewellyn, R.G.H. Greer, and D.P. Murtagh. Planet. Space Sci. **34**, 801 (1986). doi:10.1016/0032-0633(86)90076-0.
9. R.L. Gattinger, I.C. McDade, A.L. Alfaro Suzán, C.D. Boone, K.A. Walker, P.F. Bernath, W.F.J. Evans, D.A. Degenstein, J.-H. Yee, P. Sheese, and E.J. Llewellyn. J. Geophys. Res. **115**, D12, D12301 (2010). doi:10.1029/2009JD013205.
10. P.C. Cosby and T.G. Slanger. Can. J. Phys. **85**, 77 (2007). doi:10.1139/P06-088.
11. R.L. Gattinger, W.F.J. Evans, I.C. McDade, D.A. Degenstein, and E.J. Llewellyn. Can. J. Phys. **87**, 925 (2009). doi:10.1139/P09-051.
12. W.F.J. Evans, R.L. Gattinger, T.G. Slanger, D.V. Saran, D.A. Degenstein, and E.J. Llewellyn. Geophys. Res. Lett. **37**, L22105 (2010). doi:10.1029/2010GL043813.
13. P. Jenniskens, M. Lacey, B.J. Allan, D.E. Self, and J.M.C. Plane. Earth Moon Planets, **82–83**, 429 (2000).
14. T.J. Kane and C.S. Gardner. J. Geophys. Res. **98**, D9, 16875 (1993). doi:10.1029/93JD01225.
15. J.M.C. Plane. Atmos. Chem. Phys. **4**, 627 (2004). doi:10.5194/acp-4-627-2004.
16. C.S. Gardner, J.M.C. Plane, W. Pan, T. Vondrak, B.J. Murray, and X. Chu. J. Geophys. Res. **110**, D10, D10302 (2005). doi:10.1029/2004JD005670.
17. E.J. Llewellyn, N.D. Lloyd, D.A. Degenstein, R.L. Gattinger, S.V. Petelina, A.E. Bourassa, J.T. Wiensz, E.V. Ivanov, I.C. McDade et al. Can. J. Phys. **82**, 411 (2004). doi:10.1139/p04-005.
18. D.P. Murtagh, U. Frisk, F. Merino, M. Ridal, A. Jonsson, J. Stegman, G. Witt, P. Eriksson, C. Jiménez et al. Can. J. Phys. **80**, 309 (2002). doi:10.1139/p01-157.
19. A.E. Bourassa, D.A. Degenstein, and E.J. Llewellyn. J. Quant. Spectrosc. Radiat. Transf. **109**, 52 (2008). doi:10.1016/j.jqsrt.2007.07.007.
20. K.H. Becker, W. Groth, and D. Thran. Chem. Phys. Lett. **15**, 215 (1972). doi:10.1016/0009-2614(72)80152-0.
21. S.R. Langhoff, H.-J. Werner, and P. Rosmus. J. Mol. Spectrosc. **118**, 507 (1986). doi:10.1016/0022-2852(86)90186-4.
22. T.G. Slanger, P.C. Cosby, D.L. Huestis, and D.E. Osterbrock. J. Geophys. Res. **105**, D16, 20557 (2000). doi:10.1029/2000JD900256.
23. P.C. Cosby, B.D. Sharpee, T.G. Slanger, D.L. Huestis, and R.W. Hanuschik. J. Geophys. Res. **111**, A12, A12307 (2006). doi:10.1029/2006JA012023.
24. A.S.-C. Cheung, A.M. Lyyra, A.J. Merer, and A.W. Taylor. J. Mol. Spectrosc. **102**, 224 (1983). doi:10.1016/0022-2852(83)90240-0.
25. A.S.-C. Cheung, N. Lee, A.M. Lyyra, A.J. Merer, and A.W. Taylor. J. Mol. Spectrosc. **95**, 213 (1982). doi:10.1016/0022-2852(82)90248-X.
26. A.W. Taylor, A.S.-C. Cheung, and A.J. Merer. J. Mol. Spectrosc. **113**, 487 (1985). doi:10.1016/0022-2852(85)90284-X.
27. M. Barnes, M.M. Fraser, P.G. Hajigeorgiou, A.J. Merer, and S.D. Rosner. J. Mol. Spectrosc. **170**, 449 (1995). doi:10.1006/jmsp.1995.1084.
28. H.S. Son, K. Lee, S.K. Shin, and J.K. Ku. Chem. Phys. Lett. **320**, 658 (2000). doi:10.1016/S0009-2614(00)00294-3.
29. J. Lei and P.J. Dagdigian. J. Mol. Spectrosc. **203**, 345 (2000). doi:10.1006/jmsp.2000.8195.
30. G. Herzberg. *In* Molecular spectra and molecular structure I. Spectra of diatomic molecules. D. Van Nostrand Company, Inc., NewYork.
31. M. Helmer and J.M.C. Plane. J. Chem. Soc., Faraday Trans. **90**, 31 (1994). doi:10.1039/ft9949000031.
32. I.C. McDade and E.J. Llewellyn. J. Geophys. Res. **92**, A7, 7643 (1987). doi:10.1029/JA092iA07p07643.
33. S. Adler-Golden. J. Geophys. Res. **102**, A9, 19969 (1997). doi:10.1029/97JA01622.
34. I.W.M. Smith. J. Chem. Soc., Faraday Trans. **93**, 3741 (1997). doi:10.1039/a704144f.
35. B. Xue, J. Han, and H.-L. Dai. Phys. Rev. Lett. **84**, 2606 (2000). doi:10.1103/PhysRevLett.84.2606.

Appendix

Table A1. Tabulation of the simulated night airglow spectrum of the FeO orange bands in 1/10 nm wavelength bins (see Fig. 4 in main text) from 500 to 720 nm (in vacuum).

Wavelngth (nm)															
500.00	0.01	0.04	0.04	0.03	0.00	0.06	0.10	0.09	0.16	0.19	0.19	0.21	0.19	0.20	0.18
501.50	0.17	0.17	0.15	0.15	0.14	0.13	0.06	0.11	0.06	0.10	0.08	0.08	0.00	0.07	0.06
503.00	0.11	0.16	0.22	0.29	0.35	0.39	0.37	0.38	0.36	0.33	0.32	0.31	0.29	0.28	0.25
504.50	0.24	0.23	0.21	0.11	0.17	0.12	0.12	0.08	0.13	0.09	0.08	0.18	0.19	0.14	0.22
506.00	0.19	0.18	0.20	0.14	0.18	0.15	0.14	0.13	0.12	0.12	0.09	0.06	0.09	0.09	0.06
507.50	0.06	0.03	0.06	0.05	0.02	0.05	0.07	0.07	0.15	0.19	0.25	0.27	0.25	0.27	0.24
509.00	0.24	0.23	0.23	0.21	0.19	0.19	0.14	0.16	0.08	0.14	0.10	0.09	0.10	0.06	0.05
510.50	0.08	0.05	0.09	0.11	0.17	0.24	0.27	0.27	0.33	0.34	0.39	0.42	0.41	0.42	0.40
512.00	0.38	0.38	0.40	0.33	0.39	0.31	0.37	0.31	0.27	0.22	0.27	0.32	0.28	0.27	0.34
513.50	0.27	0.29	0.34	0.27	0.30	0.34	0.32	0.32	0.28	0.23	0.27	0.23	0.27	0.27	0.23
515.00	0.30	0.22	0.27	0.21	0.20	0.14	0.29	0.39	0.39	0.56	0.73	0.66	0.80	0.76	0.77
516.50	0.74	0.67	0.73	0.70	0.72	0.65	0.64	0.40	0.58	0.54	0.32	0.48	0.41	0.25	0.27
518.00	0.64	0.75	0.71	1.44	1.71	1.68	1.80	1.82	1.70	1.63	1.58	1.63	1.49	1.45	1.38
519.50	1.26	0.92	1.17	0.92	0.69	0.68	0.92	0.81	0.37	0.54	0.72	0.59	0.77	1.15	0.97
521.00	1.09	1.19	0.81	1.08	0.84	0.89	0.84	0.70	0.75	0.64	0.60	0.58	0.57	0.14	0.48
522.50	0.46	0.45	0.07	0.50	0.54	0.57	0.46	0.76	0.72	0.63	0.68	0.56	0.70	0.66	0.69
524.00	0.84	0.69	0.90	0.76	0.86	0.62	0.76	0.66	0.74	0.74	0.65	0.57	0.62	0.63	0.63
525.50	0.84	0.76	0.90	1.06	0.96	0.83	0.94	0.81	0.84	1.12	1.35	1.26	1.44	1.32	1.22
527.00	1.21	1.02	1.03	0.97	1.01	0.85	0.85	0.78	0.40	0.71	0.77	0.78	0.79	0.58	0.71
528.50	0.77	0.73	0.45	0.73	0.52	0.75	0.84	0.68	0.90	0.82	0.75	0.81	0.70	0.71	0.76
530.00	0.82	0.76	0.91	0.83	0.97	0.96	0.84	1.06	1.21	1.16	1.17	1.25	1.24	1.31	1.04
531.50	1.23	1.28	1.25	1.34	1.04	1.33	1.34	0.85	1.18	1.14	1.04	1.08	0.97	1.17	1.22
533.00	1.29	1.51	1.51	1.63	1.52	1.54	1.20	1.44	1.41	1.15	1.42	1.19	0.98	1.18	0.87
534.50	0.94	1.07	0.58	0.74	0.77	0.74	0.72	0.97	1.41	1.32	1.76	1.58	1.81	1.79	1.72
536.00	1.77	1.93	2.16	2.08	2.15	2.08	1.25	1.95	1.77	1.71	1.90	1.31	1.85	2.00	1.80
537.50	1.59	1.96	1.83	1.47	2.24	2.75	2.66	2.39	2.73	2.69	2.32	1.88	2.33	2.16	2.57
539.00	1.92	2.61	2.02	2.21	1.57	2.06	1.58	1.97	1.28	1.93	1.83	2.30	2.44	2.77	2.85
540.50	2.93	3.18	3.09	3.21	3.08	2.60	3.00	2.72	2.39	2.45	2.15	1.69	2.14	1.82	1.39
542.00	1.34	1.45	2.57	2.67	3.51	4.37	4.60	5.21	5.67	5.70	6.00	5.67	5.73	5.52	5.22
543.50	5.14	4.74	4.57	4.23	2.96	3.75	2.46	3.55	2.36	2.93	1.63	2.60	3.25	3.36	1.81
545.00	3.54	3.36	4.69	5.02	4.41	4.91	4.13	4.55	4.27	3.87	3.44	3.61	2.88	3.25	2.49
546.50	2.71	1.59	2.38	2.49	2.98	2.92	1.87	3.65	3.38	3.30	4.34	4.01	3.81	4.00	3.67
548.00	3.91	3.67	3.36	3.76	2.56	3.69	2.69	3.21	3.05	2.40	3.16	2.53	3.21	4.12	3.88
549.50	3.96	4.72	4.44	4.62	5.51	4.98	5.68	5.25	5.64	5.34	4.31	4.20	4.74	4.20	3.40
551.00	3.88	3.88	3.13	3.61	4.35	3.94	5.55	5.00	4.80	4.66	4.74	4.78	4.94	4.56	5.71
552.50	4.73	5.25	4.94	4.40	3.44	3.88	4.12	3.71	3.42	2.21	2.88	2.60	2.07	3.09	2.90
554.00	2.14	2.55	2.40	2.66	2.50	2.49	2.99	3.29	3.05	3.47	3.37	3.32	2.94	2.86	3.30
555.50	2.70	3.49	2.57	3.46	3.19	2.22	2.96	3.13	3.26	3.54	3.20	4.06	4.20	4.01	3.71
557.00	4.24	3.99	4.14	3.98	3.59	4.16	4.22	4.61	3.19	3.70	4.08	3.81	3.26	3.24	2.66
558.50	3.19	2.85	3.85	3.68	4.24	4.57	4.90	4.86	4.33	3.75	4.10	4.02	3.31	3.46	2.80
560.00	2.95	2.77	2.97	2.27	2.10	2.50	1.92	1.49	1.98	1.74	2.02	3.50	3.94	4.76	5.68
561.50	5.08	6.01	5.29	5.47	5.49	5.63	6.46	4.97	7.08	6.63	6.66	6.17	4.50	4.40	5.61
563.00	5.62	5.40	5.24	6.56	5.41	5.09	4.71	5.12	4.93	4.95	5.22	6.77	7.76	6.32	8.31
564.50	6.79	7.08	7.49	6.60	5.72	7.49	6.71	6.77	7.28	6.72	6.46	6.97	6.08	5.32	4.75
566.00	5.10	5.11	2.61	7.04	6.87	6.69	7.96	7.49	8.08	7.78	7.96	6.39	7.55	8.70	6.39
567.50	8.56	7.23	7.26	6.81	4.74	4.54	6.36	5.17	4.26	4.40	6.65	4.57	6.86	5.71	7.55
569.00	8.13	6.54	8.31	6.66	8.99	9.17	8.14	9.46	8.67	7.53	8.06	8.13	7.11	7.05	6.09
570.50	5.69	5.82	6.92	8.33	6.88	9.04	8.56	8.24	10.74	7.90	9.58	10.69	8.85	10.64	10.33
572.00	9.86	9.92	10.21	7.17	6.80	7.96	8.19	5.48	6.79	4.80	4.46	6.72	5.52	5.47	7.39
573.50	4.00	6.88	6.95	5.23	7.60	7.45	8.58	8.51	9.53	8.58	7.09	7.83	8.28	7.72	8.10
575.00	6.95	6.60	6.95	4.60	6.76	5.96	5.95	7.64	5.74	8.33	7.02	7.39	8.63	8.57	8.17
576.50	9.96	8.73	9.70	10.11	8.40	9.52	8.27	9.57	8.26	8.16	5.87	7.87	7.07	7.67	6.35
578.00	6.96	7.90	8.52	7.79	7.71	8.65	7.85	7.98	10.18	7.93	9.84	9.37	8.75	7.51	8.16
579.50	5.96	7.48	5.33	6.03	6.33	5.45	7.13	6.36	4.98	6.08	6.43	5.02	5.61	5.45	5.93
581.00	6.50	7.79	8.31	8.46	7.82	8.53	8.56	6.94	7.43	6.89	6.68	5.35	6.61	6.14	5.33
582.50	7.17	6.44	8.01	6.53	6.72	7.02	5.77	7.02	7.45	7.43	8.86	8.21	9.73	8.57	9.38
584.00	8.72	8.56	7.31	7.62	8.26	8.07	7.47	7.72	7.42	9.60	9.87	7.68	8.18	6.63	7.57
585.50	6.68	5.73	8.00	5.92	7.57	8.44	8.25	7.22	7.54	7.26	7.64	6.48	6.29	6.97	5.39
587.00	7.75	8.69	8.34	9.31	7.13	8.00	8.34	7.86	6.01	7.15	5.82	4.61	7.18	4.92	6.52
588.50	4.86	5.39	5.19	5.88	5.48	5.09	8.53	6.52	8.45	7.64	10.39	9.57	9.89	8.89	8.76
590.00	9.01	8.16	8.34	6.48	8.89	7.85	8.74	6.26	7.04	8.46	7.88	6.25	7.56	7.96	8.56

Table A1 (*continued*).

Wavelngth (nm)															
591.50	9.41	7.94	8.88	10.68	10.56	9.83	9.66	10.40	11.13	11.96	12.45	13.54	10.68	14.26	13.40
593.00	13.52	11.03	12.77	11.14	11.46	12.17	13.82	11.79	13.08	13.10	10.78	11.60	12.38	10.70	11.31
594.50	9.02	10.88	13.10	9.82	12.51	8.85	10.96	11.19	9.56	11.07	8.03	9.84	9.44	8.13	10.86
596.00	10.45	10.20	10.57	10.78	12.70	8.09	10.54	10.82	8.03	10.45	10.37	11.34	12.39	10.72	10.89
597.50	12.85	12.20	10.50	10.21	11.36	8.09	9.79	10.82	9.54	10.97	11.04	7.39	11.19	11.49	10.08
599.00	6.72	9.94	7.67	10.72	10.83	9.24	13.69	13.99	14.53	13.95	13.41	15.14	11.73	13.60	13.26
600.50	12.49	14.12	14.33	10.13	13.36	13.40	13.91	8.12	12.50	11.97	9.51	10.30	9.62	7.76	10.92
602.00	10.38	10.85	8.50	10.45	9.08	8.63	10.26	8.44	9.55	8.99	9.12	9.34	9.56	7.17	8.08
603.50	8.18	8.99	6.57	9.49	8.94	7.46	9.64	10.06	9.38	8.13	8.05	7.52	7.66	7.25	8.34
605.00	7.67	8.53	7.98	7.58	6.32	8.35	6.19	7.48	5.90	6.56	7.41	8.87	8.59	8.68	8.65
606.50	7.86	8.72	8.74	6.69	8.12	8.07	8.17	6.95	8.95	7.59	9.41	6.89	7.15	7.67	8.67
608.00	5.09	6.94	7.82	7.24	7.96	8.59	6.00	8.48	7.27	7.36	5.50	8.36	6.59	7.05	8.05
609.50	7.34	7.87	6.89	6.68	7.36	6.98	5.76	6.67	5.87	6.83	5.94	8.23	8.29	9.70	7.06
611.00	8.70	8.25	7.56	8.51	8.77	8.80	8.53	7.95	8.71	8.71	9.14	8.32	7.17	7.86	7.80
612.50	6.01	6.90	6.07	6.43	8.06	7.39	7.29	8.07	7.08	7.63	6.35	7.86	5.75	6.92	6.45
614.00	5.22	7.27	6.57	6.71	6.36	6.80	7.13	5.66	6.56	5.65	5.10	5.19	4.49	6.48	5.93
615.50	5.98	5.80	5.81	7.12	6.05	7.08	6.13	6.32	5.59	5.82	6.20	4.94	5.63	4.86	5.83
617.00	5.66	5.37	4.10	4.40	5.94	2.83	5.75	5.20	5.08	5.62	5.01	5.51	6.06	5.78	5.27
618.50	6.31	4.86	5.72	4.98	4.59	3.97	3.93	2.81	4.62	3.43	3.90	3.51	3.13	3.65	3.75
620.00	4.97	4.05	4.98	4.65	5.95	6.05	5.84	6.57	5.81	6.06	6.59	6.16	6.21	6.70	6.62
621.50	6.88	5.63	6.04	6.40	3.93	5.31	5.51	3.94	4.66	5.87	4.98	5.99	7.38	7.03	7.87
623.00	6.99	7.31	6.81	6.92	6.67	6.68	6.75	7.57	7.06	7.35	4.62	6.91	6.66	6.59	4.24
624.50	6.48	7.10	5.39	7.12	7.59	7.56	7.63	7.74	8.73	7.35	7.77	7.06	6.92	6.00	6.70
626.00	5.62	6.30	6.40	5.35	6.51	5.33	5.70	6.57	6.01	4.82	6.84	6.85	6.21	7.70	6.97
627.50	8.02	6.37	7.11	7.54	6.63	6.29	5.63	7.43	5.18	7.35	7.55	9.05	5.61	9.05	8.35
629.00	6.53	7.67	7.80	6.55	6.46	6.42	5.14	6.47	6.62	7.21	5.67	7.31	6.76	7.20	6.01
630.50	7.91	6.24	6.68	8.71	7.09	6.94	8.16	8.27	7.88	7.07	8.02	7.26	5.46	7.42	4.04
632.00	6.67	7.01	4.96	7.24	6.40	8.46	7.56	8.10	8.88	8.82	7.44	8.89	6.80	6.74	7.55
633.50	5.69	7.37	5.26	6.54	5.85	5.74	5.88	6.77	5.57	6.25	6.42	6.01	6.69	6.34	7.79
635.00	6.78	7.29	7.31	8.12	8.31	8.02	6.54	8.28	7.02	6.53	5.83	6.49	5.94	5.63	5.73
636.50	6.12	6.41	6.88	7.78	5.97	7.50	6.71	6.51	7.24	6.82	5.96	6.66	5.49	6.08	5.32
638.00	5.82	4.76	5.94	5.52	4.67	4.81	5.92	3.97	6.64	6.80	5.68	7.38	6.84	8.20	7.18
639.50	7.98	8.25	7.89	7.32	7.98	6.78	5.78	7.35	6.90	6.74	5.49	5.93	5.71	5.07	6.30
641.00	6.49	7.43	6.23	7.15	7.64	7.67	7.98	7.69	7.04	8.52	6.45	7.92	6.08	6.42	6.47
642.50	7.11	5.84	6.18	6.63	7.29	6.29	7.99	6.75	6.71	6.53	6.18	6.64	7.12	6.64	5.64
644.00	7.08	6.16	6.02	5.17	6.12	5.04	5.51	3.51	4.67	5.26	3.69	5.68	5.62	5.11	5.17
645.50	5.68	6.78	5.05	6.05	5.41	5.32	5.26	5.32	4.91	5.93	6.30	5.00	4.98	5.70	5.54
647.00	3.75	5.93	4.64	4.25	3.79	5.34	4.20	4.41	4.61	5.23	5.92	4.44	5.29	4.79	3.77
648.50	4.36	4.42	3.49	2.98	3.56	4.35	3.32	3.59	3.57	4.34	3.57	4.64	4.28	4.57	4.04
650.00	5.02	3.24	5.12	2.71	4.63	4.19	4.30	3.88	4.37	4.20	3.91	3.76	3.70	2.47	3.47
651.50	2.70	3.26	3.72	3.21	4.72	4.95	6.17	4.39	5.82	5.66	4.16	5.32	4.14	4.46	4.38
653.00	3.41	4.00	2.99	3.61	2.96	3.28	3.79	3.21	3.14	4.14	3.60	4.75	4.43	4.71	4.11
654.50	4.79	5.38	4.94	4.13	4.89	4.40	3.86	4.05	4.03	3.84	4.16	3.45	3.06	3.79	3.70
656.00	2.82	3.45	4.79	2.79	4.65	3.56	4.69	4.34	4.17	3.79	3.68	4.23	2.87	3.99	3.04
657.50	4.18	3.56	4.17	3.20	4.05	4.23	3.98	3.84	3.02	3.56	3.70	3.97	3.51	4.08	3.65
659.00	4.57	3.87	4.27	4.06	4.34	4.35	4.92	3.31	4.77	3.39	3.64	3.72	3.73	3.75	4.53
660.50	3.32	3.88	3.38	3.83	3.51	4.23	3.84	5.73	3.89	5.67	5.26	5.58	5.17	5.84	5.25
662.00	5.17	3.74	5.36	3.68	5.05	3.51	4.14	5.12	4.40	4.67	5.36	4.39	6.31	5.29	5.31
663.50	6.00	5.41	5.70	4.87	5.04	4.66	5.52	4.43	5.19	4.89	6.32	4.48	5.54	5.34	4.49
665.00	4.98	5.96	4.71	4.51	5.28	6.48	6.25	6.80	6.02	7.71	4.49	7.57	5.52	5.95	6.52
666.50	4.65	4.40	3.86	6.76	5.57	6.16	4.88	7.27	6.02	5.56	7.11	5.63	5.16	5.41	4.02
668.00	6.28	5.73	5.81	5.01	6.34	5.74	7.15	5.36	6.37	6.46	5.45	7.39	6.58	6.49	4.57
669.50	7.05	5.92	4.67	6.41	4.82	4.66	5.66	5.25	4.11	5.02	5.28	3.75	4.96	5.59	5.46
671.00	5.27	5.38	5.34	5.56	6.23	4.92	5.73	4.63	5.07	4.50	5.44	3.83	3.81	4.75	4.28
672.50	4.35	4.38	5.62	5.21	4.81	6.24	5.35	5.88	5.71	5.49	4.91	5.28	4.93	5.52	4.36
674.00	4.25	3.46	4.57	4.59	4.24	5.45	4.42	6.12	4.43	6.62	5.70	5.13	6.41	5.82	5.62
675.50	4.77	5.05	5.28	4.52	4.90	5.57	4.27	4.39	4.99	4.12	5.37	4.51	3.51	5.58	4.24
677.00	4.56	3.94	5.05	4.08	4.97	4.52	4.71	4.47	4.70	4.33	3.74	4.34	3.14	4.33	3.41
678.50	4.63	3.58	4.56	3.33	4.80	4.30	4.87	4.88	4.96	4.52	4.57	4.63	4.22	4.19	2.29
680.00	4.53	3.10	3.86	3.40	4.64	3.33	4.80	4.14	4.40	3.79	4.41	3.65	3.60	4.26	1.86
681.50	3.78	2.09	3.96	2.40	2.89	3.13	2.92	2.09	3.21	2.69	2.56	3.22	1.96	3.14	2.64
683.00	2.61	2.53	3.33	2.71	2.84	3.11	3.20	2.56	2.58	2.29	2.70	1.99	1.92	2.86	1.28
684.50	3.31	2.57	3.53	2.79	3.05	3.14	3.38	2.94	3.05	2.22	2.43	2.66	2.63	2.58	1.89

Table A1 (*concluded*).

Wavelngth (nm)														
686.00	2.92	3.05	2.95	2.22	3.81	2.92	3.23	3.14	3.29	3.11	3.23	2.94	2.52	2.12	2.45
687.50	3.16	2.77	3.45	3.34	3.14	3.41	3.40	3.06	3.17	2.45	3.05	2.63	2.14	2.96	2.00
689.00	3.67	2.54	3.36	3.43	3.64	3.45	3.70	3.76	3.28	3.53	2.79	3.35	3.86	3.29	4.06
690.50	3.79	2.76	3.50	3.76	2.79	2.81	3.00	3.89	3.17	3.30	2.40	3.59	4.21	2.64	4.61
692.00	3.61	3.85	3.56	3.18	3.96	3.75	2.99	3.15	2.41	3.30	2.60	3.53	2.08	4.03	3.65
693.50	4.04	3.59	4.83	2.96	4.06	4.14	3.70	4.09	3.21	3.66	2.88	2.39	4.72	3.17	3.63
695.00	3.75	4.02	2.93	3.87	3.21	4.63	3.22	3.86	4.07	2.61	4.09	3.61	3.72	3.05	4.38
696.50	4.22	3.33	4.90	3.02	4.71	3.60	4.03	4.44	5.02	4.56	4.77	5.36	3.89	6.11	3.69
698.00	4.38	4.54	4.88	3.13	4.81	2.23	4.34	3.92	3.92	4.61	4.43	4.80	4.60	4.16	5.15
699.50	4.16	5.06	3.94	3.83	5.10	3.89	3.34	4.51	4.85	3.67	5.49	5.15	4.58	5.15	4.71
701.00	5.78	5.69	4.39	4.41	4.07	4.28	4.15	3.77	3.89	4.96	5.41	4.23	5.88	5.53	5.91
702.50	4.78	6.37	5.57	5.08	4.67	3.69	4.91	4.66	4.74	2.56	5.42	4.68	3.91	6.33	5.59
704.00	5.39	6.83	6.10	7.25	6.00	6.99	6.12	5.62	6.32	5.60	4.10	5.01	5.59	4.65	4.82
705.50	5.51	5.67	6.13	5.07	5.88	5.29	5.72	5.10	5.09	5.07	4.57	4.15	4.44	5.08	4.07
707.00	3.78	4.56	5.60	4.12	6.23	4.11	4.96	5.59	4.32	4.55	3.94	4.94	4.64	3.32	5.41
708.50	3.27	3.48	5.16	3.86	5.16	4.31	5.26	4.81	4.88	4.07	5.34	3.55	4.04	3.82	5.11
710.00	4.29	4.04	2.60	5.42	4.44	4.37	5.19	5.20	5.92	5.52	5.33	6.35	5.58	5.23	6.00
711.50	6.25	4.54	5.35	4.96	6.06	4.14	4.94	5.59	4.70	4.59	5.68	4.93	4.91	5.19	4.09
713.00	4.72	4.64	4.23	4.53	4.71	3.69	3.49	3.96	3.55	3.22	4.44	4.65	4.15	4.87	4.07
714.50	4.91	4.55	4.81	4.00	3.94	3.97	2.63	4.44	2.78	3.26	3.31	3.67	3.07	3.82	4.54
716.00	4.38	4.65	3.97	5.19	3.89	3.82	4.11	4.06	3.24	2.93	3.15	3.63	2.71	4.13	3.73
717.50	3.54	4.11	3.21	4.86	4.23	3.52	4.09	2.96	3.95	2.01	4.30	2.60	3.24	2.01	2.22
719.00	2.29	2.34	3.09	1.93	3.15	2.15	2.53	2.28	2.80	2.24	2.36				

Note: The initial wavelength for each row in the table is the first entry in the row.

This article has been cited by:

1. GattingerR.L., EvansW.F.J., LlewellynE.J.. 2011. Chemiluminescent NiO* emissions: band systems and spectral simulation. *Canadian Journal of Physics* **89**:8, 869-874. [Abstract] [Full Text] [PDF] [PDF Plus]